# Multiple Mode Couplings in a Waveguide Array for Broadband Near-Zero Dispersion and Supercontinuum Generation

Saleha Fatema , Md Borhan Mia, Student Member, IEEE, and Sangsik Kim, Senior Member, IEEE, Senior Member, OSA

Abstract—We achieve a broadband near-zero dispersion in a thin silicon nitride waveguide array at near-infrared utilizing the multiple mode couplings. Different orders of modes are coupled at four different wavelengths, generating eight zero dispersion wavelengths (ZDWs). The broadband near-zero dispersion profile within 90 ps/nm/km is achieved, spanning over the spectral range of 1350—1900 nm. Using the dispersion engineered waveguide array, an octave-spanning supercontinuum is numerically generated with a pump of 100 fs and 200 pJ. The concept of using multiple mode couplings to obtain broadband near-zero dispersion can be applied to other spectral regimes and material platforms as well, by engineering the structural parameters to shift the positions of the ZDWs.

Index Terms—Dispersion engineering, integrated optics, supercontinuum.

#### I. INTRODUCTION

UPERCONTINUUMS (SCs) can produce a broadband optical spectrum, and they have been used in a wide range of applications such as coherent spectroscopy [1], frequency metrology [2], pulse compression [3], exotic nonlinear dynamics [4], and optical coherence tomography [5]. While SC generating devices have been widely developed with tabletop [6] and optical fiber [7] systems, recent advances in nanotechnology have realized SC generation on chip-scale photonic devices [8]–[23]. Photonic chips can boost the nonlinear optical processes with increased optical intensity, while the tiny chip-scale platform ensures a more portable, robust, and low-cost system.

The extensive spectral broadening of an SC pulse arises from the interaction of several nonlinear processes [8]. The strength of nonlinear interplay depends on the nonlinear phase shift  $\phi_{\rm NL}=\gamma PL$ , where  $P,\ L$ , and  $\gamma$  are the pulse energy, interaction length, and nonlinear coefficient, respectively, and one can increase either  $L,\ P,$  or  $\gamma$  to increase  $\phi_{\rm NL}$ . However,

Manuscript received May 29, 2020; revised September 20, 2020; accepted September 22, 2020. Date of publication September 24, 2020; date of current version January 2, 2021. This work was supported by the National Science Foundation under Grant ECCS-1930784. (Corresponding author: Sangsik Kim.)

The authors are with the Department of Electrical and Computer Engineering, Texas Tech University, Lubbock, Texas 79409 USA (e-mail: saleha.fatema56@gmail.com; mborhan.mia@ttu.edu; sangsik.kim@ttu.edu).

Color versions of one or more of the figures in this article are available online at https://ieeexplore.ieee.org.

Digital Object Identifier 10.1109/JLT.2020.3026634

increasing L often introduces a high optical loss and dispersion issues, and the damage threshold limits increasing P. Therefore, for a large  $\phi_{\rm NL}$ , increasing the nonlinear coefficient  $\gamma$ is highly desired. The nonlinear coefficient is defined by  $\gamma =$  $(2\pi n_2)/(A_{\text{eff}}\lambda)$ , where  $n_2$ ,  $\lambda$ , and  $A_{\text{eff}}$  are the nonlinear index, vacuum wavelength, and effective modal area, respectively. The obvious approach to increase  $\gamma$  is to select a material with a high  $n_2$ , and various material platforms such as indium gallium phosphide [9], chalcogenide glasses [10], titanium dioxide [11], germanium [12], aluminum nitride [13], and lithium niobate [14] have been investigated for on-chip SC generation. Silicon (Si), which is compatible with the CMOS process, also has a high nonlinear index  $(n_2 = 5 \times 10^{-18} \,\mathrm{m}^2 \,\mathrm{W}^{-1})$ , and a couple of on-chip SC generation have been demonstrated [15], [16]. However, due to a high two-photon absorption (TPA) coefficient, the conversion efficiency is low, and an achievable spectral bandwidth is limited [17]. To avoid the large TPA of Si, silicon nitride (Si<sub>3</sub>N<sub>4</sub>) has been widely used as a material platform for on-chip nonlinear processes [18]-[28]. Silicon nitride waveguides show a low linear propagation loss over broad spectral regions (400 nm - 4600 nm) [24], [25],allowing high-Q (over 10) million) microresonators [26]–[28]. The large bandgap ( $\approx$  5 eV) of Si<sub>3</sub>N<sub>4</sub> allows nonlinear interactions that are free from TPA, and moderately large nonlinearity ( $n_2 = 2.5 \times 10^{-19} \,\mathrm{m}^2 \,\mathrm{W}^{-1}$ [25]) and a high refractive index of Si<sub>3</sub>N<sub>4</sub> help to achieve a high  $\gamma$ . Leveraging all these properties, SC spectra broader than an octave have been demonstrated from visible to mid-infrared. The absence of substantial Raman gains in Si<sub>3</sub>N<sub>4</sub> also assists in generating coherent SCs with lower energies [22], [23].

For an extreme spectral broadening of an SC, the phase matching of the parametric process over a broad bandwidth is of utmost importance, which requires careful dispersion engineering. A broadband near-zero dispersion profile with multiple zero dispersion wavelengths (ZDWs) is highly desired to extend the bandwidth of an SC, and a couple of structures have been proposed [29]–[34]. However, the proposed structures are complicated and are not CMOS compatible. In the Si<sub>3</sub>N<sub>4</sub> platform, a thick film thickness (>800 nm) is typically required for near-zero or anomalous dispersions at near-infrared (near-IR) [26]–[28]. However, due to the high film stress, such a thick Si<sub>3</sub>N<sub>4</sub> film is easy to crack [26]–[28], and the current CMOS process limits the Si<sub>3</sub>N<sub>4</sub> thickness to less than 300 nm, which shows a highly normal dispersion in the infrared. Thus,

TABLE I
COMPARISON OF NEAR-ZERO DISPERSIONS WITH MULTIPLE ZDWS:
EXPERIMENTAL [23] AND NUMERICAL [29]–[34]

Ref.	Wavelengths (nm)	Materials & Structure	Thickness (nm)	Dispersion (ps/nm/km)	# of ZDWs
[23]	700 - 900	Si <sub>3</sub> N <sub>4</sub>	300	±150	2
[29]	1300 - 1550	Si strip	425	$\pm 400$	2
[30]	1526 - 2624	Si+slot (Si-nc)	400	-24 to 22	4
[31]	1562 - 2115	Si+slot (Si-nc)	825	±16	3
[32]	1461 - 2074	Si+slot (SiO <sub>2</sub> )	520	-20 to $22$	4
[33]	1660 - 3290	TiO2/SiN	1965	-4.7 to 5.7	4
[34]	2030 - 5030	Si/Al <sub>2</sub> O <sub>3</sub> /SiN	2382	-3.6 to $5.1$	6
This work	1350-1900	$Si_3N_4$	300	±90	8

further advanced dispersion engineering is required to develop a fully CMOS compatible on-chip SC generation device.

In an on-chip platform, the waveguide cross-sections can be engineered to control the dispersions of the guided mode; in general, the waveguide dispersion approaches anomalous as the modal confinement increases (with a larger cross-section) and normal near the cut-off (with a smaller cross-section). Note that, however, the overall dispersion is a combination of both modal and material dispersions, and the intrinsic material dispersion limits the achievable dispersion range. To overcome the material dispersion limit, a mode-coupling approach has been explored in several waveguides and resonator structures [35]-[41]. A mode-coupling appears when two different modes are close by and coupled together, resulting in symmetric and anti-symmetric supermodes. The coupled modes force the symmetric and antisymmetric modes toward normal and anomalous dispersions, respectively. The degree of shift can be controlled by their coupling strength, which depends on the separation distance between the two modes. Such mode-couplings can be formed between bending radiuses [35], [36], different mode orders [37], [38], polarizations [39], and materials [40], [41].

In this paper, we introduce multiple mode couplings in a 300 nm-thick CMOS compatible silicon nitride waveguide array to achieve a broadband near-zero dispersion (NZD) at nearinfrared. This paper is an extension of our previous work [38]. Based on the concept of multiple mode couplings, we systematically achieve broadband near-zero dispersions for the generations of supercontinuums. Four mode couplings with eight ZDWs are introduced on a thin silicon nitride, which shows highly normal dispersion unless otherwise engineered. Table I summarizes the previous near-zero dispersion designs with multiple ZDWs. We numerically examined the SC generation utilizing this dispersion profile and the high nonlinearity of the silicon nitride waveguide. The closely spaced ZDWs help the generations of multiple dispersive waves (DWs), enabling octave-spanning SCs by pumping at both normal and anomalous dispersion regions in the near-infrared.

## II. DISPERSION ENGINEERING WITH MULTIPLE MODE COUPLINGS IN A WAVEGUIDE ARRAY

The cross-section of the proposed structure, along with the geometric parameters, is presented in Fig. 1. An array of five silicon nitride waveguides (blue) are cladded in SiO<sub>2</sub> (gray).

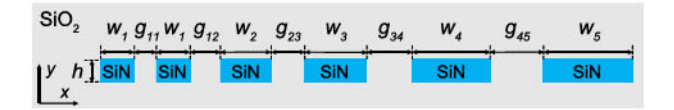


Fig. 1. Schematic of the proposed structure (blue:  $\mathrm{Si}_3\mathrm{N}_4$ , gray:  $\mathrm{Si}_0\mathrm{N}_2$ ). The thickness of the waveguides are set to h=300 nm. The widths  $w_i$  and gap sizes  $g_{ij}$  are optimized to  $w_1=805$  nm,  $w_2=1080$  nm,  $w_3=2560$  nm,  $w_4=4000$  nm, and  $w_5=5510$  nm, and gaps are  $g_{11}=120$  nm,  $g_{12}=525$  nm,  $g_{23}=750$  nm,  $g_{34}=1620$  nm, and  $g_{45}=2240$  nm.

The height of the waveguides is set to  $h=300~\rm nm$  to leverage the CMOS compatibility. The waveguide array starts with a single slot waveguide, formed by the first two silicon nitride waveguides (with  $w_1$ - $g_{11}$ - $w_1$  at the leftmost side), followed by a series of waveguides with a gradual increment in their width. The slot waveguide mode  ${\rm TE_{slot}}$  has a faster group velocity compared to the other transverse electric (TE) modes and helps to achieve a sharp rise in dispersion. The widths of the waveguides after the slot waveguide are increased one after the other so that a consecutive order of modes can be assigned. The fundamental  ${\rm TE}\,({\rm TE}_0)$  mode is placed in the waveguide with the width  $w_2$ , then the first-order  ${\rm TE}\,({\rm TE}_1)$  mode in the waveguide with  $w_3$ , followed by the second-order  ${\rm TE}\,({\rm TE}_2)$  mode in the waveguide with  $w_4$ , and lastly, the third-order  ${\rm TE}\,({\rm TE}_3)$  mode in the waveguide with  $w_5$  [38].

The widths of the waveguides are optimized so that each mode of a waveguide couples to the nearest waveguide modes at distinct wavelengths. If the effective refractive indices  $(n_{\text{eff}})$  of two adjacent modes are equal, the waveguides couple together, forming two super modes, i.e., a symmetric and an anti-symmetric mode [40], [41]. Fig. 2(a) and 2(b) show the simulated  $n_{\rm eff}$  and the corresponding dispersions D, respectively, when we consider the mode coupling between the TE<sub>slot</sub> and TE<sub>0</sub> modes only: independent TE<sub>slot</sub> (orange dashed) and TE<sub>0</sub> (blue dashed) modes without coupling, and coupled symmetric (orange solid) and anti-symmetric (blue solid) modes. Note that, in Fig. 2(a), the  $n_{
m eff}$  of the  ${
m TE}_{
m slot}$  mode (orange dashed) matches that of the TE<sub>0</sub> mode (blue dashed) at a certain wavelength ( $\lambda \approx 1420 \text{ nm}$ ); once we locate these two modes together (here, with the  $g_{12} =$ 525 nm), they couple together, resulting in symmetric (orange solid) and anti-symmetric (blue solid) modes. These supermodes try to avoid the mode crossing, forcing the symmetric mode to a normal dispersion (D < 0) and the anti-symmetric mode to an anomalous dispersion (D > 0); this property is clearly seen in Fig. 2(b). Notice that the dispersion of the anti-symmetric mode (blue solid line) exhibits a near-zero dispersion (zoomed-in), while the other dispersions are highly normal. Since our goal is to shift the normal dispersion of a thin silicon nitride waveguide mode to a NZD, we will use this anti-symmetric mode for our dispersion.

The peak dispersions  $D^{\pm}_{peak}$  and the bandwidth  $\delta\omega$  of the coupled symmetric  $(D^{+}_{\omega})$  and anti-symmetric  $(D^{-}_{\omega})$  modes can be represented as follows [40], [41],

$$D_{peak}^{\pm} = D_0 \pm \frac{1}{4|\kappa|} \left(\frac{1}{\nu_1} - \frac{1}{\nu_2}\right)^2 \tag{1}$$

$$\delta\omega = 2|\kappa| \left| \frac{1}{\nu_1} - \frac{1}{\nu_2} \right|^{-1} \tag{2}$$

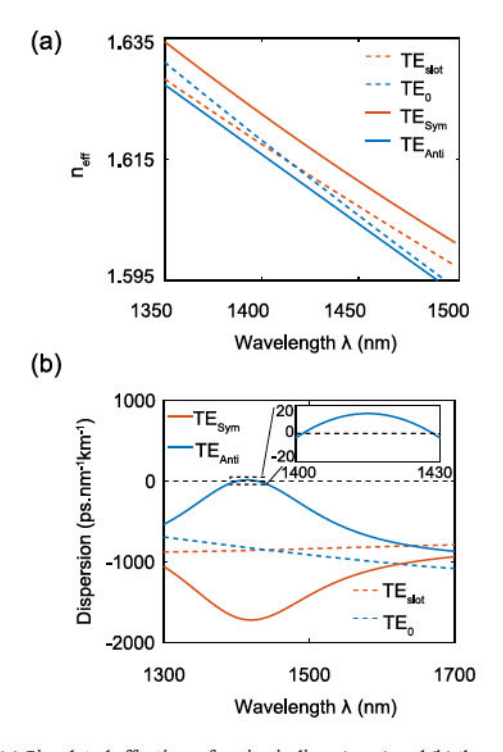


Fig. 2. (a) Simulated effective refractive indices ( $n_{\rm eff}$ ) and (b) the corresponding dispersion profiles of each mode: independent  ${\rm TE_{slot}}$  (orange dashed) and  ${\rm TE_0}$  (blue dashed) modes without coupling, and the coupled symmetric (orange solid) and anti-symmetric (blue solid) modes. The inset in (b) shows the zoomed-in view of the NZD region.

where,  $\nu_1$  and  $\nu_2$  are the group velocity of the two independent modes without coupling, and  $\kappa$  is the coupling coefficient between them. The group velocity dispersion (GVD) of the two independent modes are assumed to be equal to  $D_0$ . Notice that, in Eq. (1), the magnitudes of the peak dispersions are inversely proportional to  $\kappa$ . The  $\kappa$  can be tuned by adjusting the spacing  $g_{ij}$ ; i.e., a larger gap size reduces  $\kappa$ , increasing the magnitude of peak dispersions, and it is the opposite for a smaller gap. Also, there exists a trade-off between the peak values in dispersion (Eq. (1)) and the bandwidth (Eq. (2)); i.e., a weaker coupling induces a higher dispersion peak but a narrower bandwidth, and it is the opposite for a stronger coupling. Since our goal is to achieve a broadband NZD to overcome the strong normal dispersion of a thin silicon nitride waveguide at near-infrared, we used coupling coefficients that are small enough to show slight anomalous dispersion but as large as possible to achieve a broader bandwidth. To extend the near-zero dispersion bands further, we also introduce mode couplings multiple times at different wavelengths by cascading waveguides in an array.

To engineer the specific waveguide widths, we first fixed the geometric parameter for the slot waveguide ( $w_1 = 805$  nm and  $g_{11} = 120$  nm). Then the  $n_{\rm eff}$  of  ${\rm TE_{slot}}$  mode is plotted as a function of wavelength, along with the  $n_{\rm eff}$  of the  ${\rm TE_{0}}$  mode with different widths [38]. The  $n_{\rm eff}$  profile of the  ${\rm TE_{slot}}$  mode intersects (i.e., gets matched with) the  $n_{\rm eff}$  profile of the  ${\rm TE_{0}}$  mode allotted in different waveguide widths at different wavelengths. Therefore, if one fixes the desired coupling wavelength, the width required for the coupling can be found. As

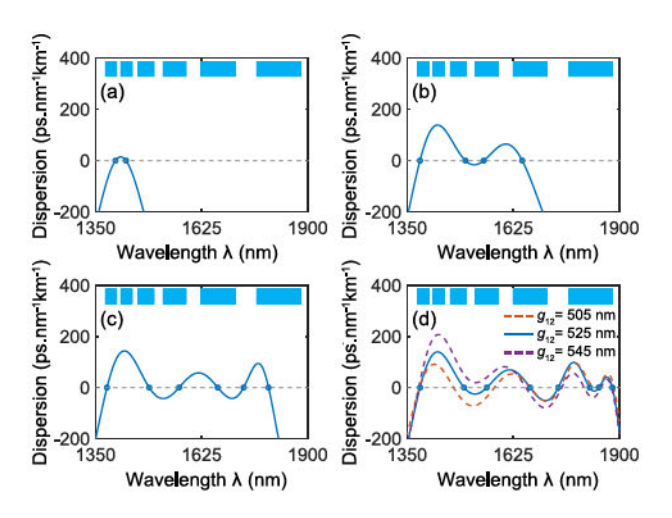


Fig. 3. The evolution of NZD profile by cascading waveguide array: mode couplings between (a)  $TE_{\rm slot}$  and  $TE_0$ , (b)  $TE_{\rm slot}$ - $TE_0$  and  $TE_1$ , (c)  $TE_{\rm slot}$ - $TE_0$ - $TE_1$  and  $TE_2$ , and (d)  $TE_{\rm slot}$ - $TE_0$ - $TE_1$ - $TE_2$  and  $TE_3$ . Insets show the cascaded waveguide array. In (d), the peak dispersion is varied by changing the gap:  $g_{12}=505$  nm (orange dashed) and  $g_{12}=545$  nm (purple dashed). The other geometric parameters are the same as in Fig. 1.

our goal is to engineer dispersion at near-infrared, we selected the first coupling wavelength as  $\lambda_1 \approx 1420$  nm. The width of the waveguide containing the  $TE_0$  mode for which the  $n_{\text{eff}}$  is equal to that of the  $TE_{slot}$  mode is found to be  $w_2 = 1080$  nm. If a coupling wavelength is required to be less than 1420 nm, one can simply reduce the waveguide width to match the  $n_{\rm eff}$ of the TE<sub>0</sub> mode at a shorter wavelength. Similarly, to achieve the mode coupling at a wavelength longer than 1420 nm, one can increase the  $w_2$ . Fig. 3(a) shows the dispersion profile of the anti-symmetric mode by coupling the TE<sub>slot</sub> and TE<sub>0</sub> modes; it clearly shows a near-zero dispersion near the coupling wavelength  $\lambda_1 = 1420$  nm. The gap size  $g_{12}$  is optimized to introduce the slightly anomalous but close to near-zero dispersion. The same approach is followed to determine the widths and gaps of the next waveguides. In Fig. 3(a), the dispersion turns back to the normal region after the coupling wavelength. To leverage this regime to the near-zero dispersion, the next coupling is introduced at  $\lambda_2 = 1605$  nm by coupling the TE<sub>0</sub> and  $TE_1$  modes. At this wavelength, the  $n_{\rm eff}$  of the  $TE_0$  mode (at  $w_2 = 1080 \,\mathrm{nm}$ ) matches that of the TE<sub>1</sub> mode at  $w_3 = 2560 \,\mathrm{nm}$ . This mode coupling results in the second peak of the dispersion profile, as depicted in Fig. 3(b). We repeated the steps to add two additional mode couplings at  $\lambda_3 = 1770$  nm and  $\lambda_4 = 1870$  nm, and optimized the waveguide widths for the  $TE_2$  and  $TE_3$  modes as  $w_4 = 4000$  nm and  $w_5 = 5510$  nm, respectively, with the gap sizes of  $g_{34} = 1620$  nm and  $g_{45} = 2240$  nm. The evolutionary dispersion profiles with the introduction of additional TE2 and TE<sub>3</sub> modes are plotted in Fig. 3(c) and 3(d), respectively. With further optimization, the dispersion profile can be flattened further, for example, by optimizing the coupling strength via the gap between the waveguides. In Fig. 3(d), the effect of varying the coupling strength by changing the gap size is shown; by reducing the gap  $g_{12}$  by 20 nm (i.e., 505 nm, orange dashed), the peak dispersion can be reduced to below 90 ps/nm/km, and similarly,

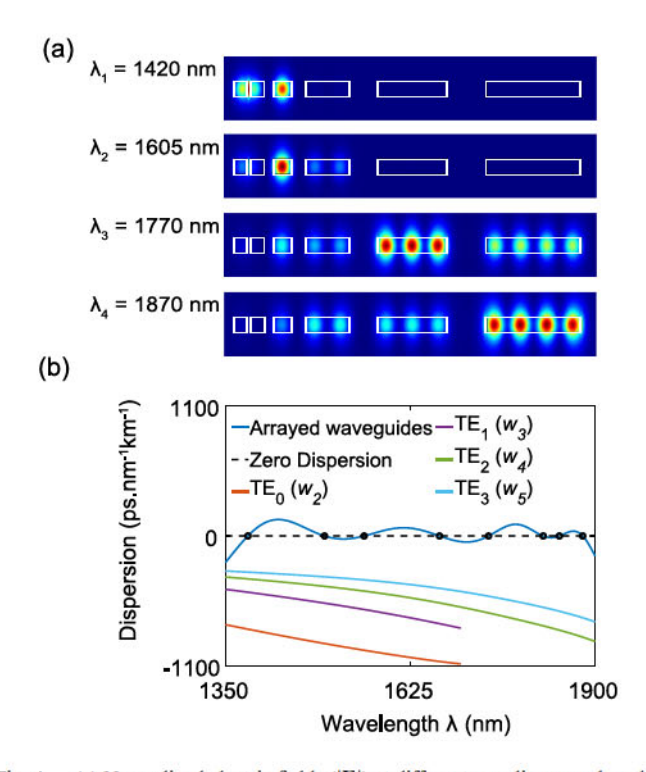


Fig. 4. (a) Normalized electric fields (|E|) at different coupling wavelengths:  $\lambda_1=1420\,\text{nm}, \lambda_2=1605\,\text{nm}, \lambda_3=1770\,\text{nm}, \text{and}\,\lambda_4=1870\,\text{nm}$ . (b) Overall dispersion profile with four mode couplings (blue solid). The dashed black line denotes the zero-dispersion, and the circles indicate the ZDWs. The dispersions of individual modes, when they are isolated, are also plotted:  $TE_0$  (orange),  $TE_1$  (purple),  $TE_2$  (green), and,  $TE_3$  (cyan).

increasing the  $g_{12}$  by 20 nm (i.e., 545 nm, purple dashed) can increase the dispersion peak to 207 ps/nm/km.

Fig. 4(a) shows the mode profiles (|E|) at different coupling wavelengths and clearly shows the couplings between different orders of modes. The blue solid line in Fig. 4(b) shows the final dispersion. The black circles denote the positions of the ZDWs, and eight ZDWs have been obtained. The dispersion profiles of each mode, when they are isolated, are also plotted to compare:  $TE_0$  (orange),  $TE_1$  (purple),  $TE_2$  (green), and  $TE_3$  (cyan). The discontinuities in TEo and TE1 are due to the modal cut-off at longer wavelengths. Notice that every mode shows a highly normal dispersion (<-300 ps/nm/km) in the given spectral region when each waveguide is separated. Due to this high normal dispersion, thin (h < 300 nm) silicon nitride waveguides are not suitable for many nonlinear applications such as SC and Kerr combs generation at NIR. Here the multiple mode couplings can result in multiples of the anomalous dispersion peaks that lead to a broadband NZD profile, as shown in Fig. 4(b). For the excitation of a specific mode, we can use an adiabatic mode transition to effectively couple to the desired pump mode [35], [42].

## III. DISPERSIVE WAVES WITH MULTIPLE MODE COUPLINGS

To extend the bandwidth of an SC, the generation of dispersive waves (DWs) is highly desired [7], [25]. A DW generation, also commonly known as Cherenkov radiation [43], results from a

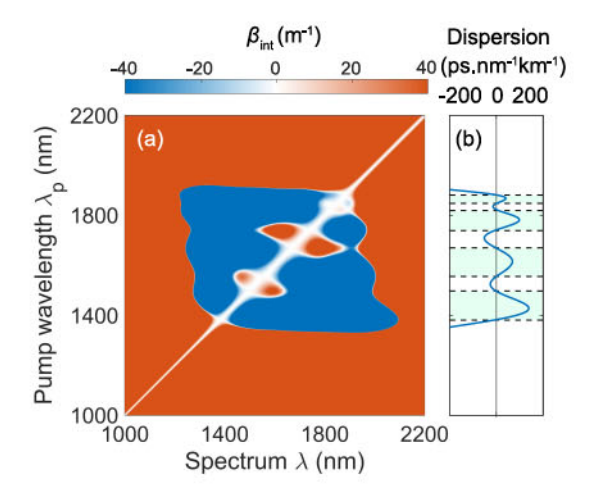


Fig. 5. (a) Map of the integrated dispersion  $\beta_{\rm int}$  as functions of the spectrum  $\lambda$  (x-axis) and the pump wavelength  $\lambda_p$  (y-axis). The diagonal white line indicates the pump wavelength. The rest of the white lines (i.e., discontinuity of blue and orange colors) correspond to the wavelengths at which the  $\beta_{\rm int}=0$  and dispersive waves are generated. (b) Dispersion curve of the waveguide array. The anomalous dispersion region is shaded with the green color. The black solid line denotes the zero-dispersion and the dashed lines are the spectral positions of the zero dispersion wavelengths (ZDWs).

phase-matching in the presence of higher-order dispersions, and it can transfer the energy to a wavelength away from the pump across the ZDW [25], [44]. The presence of more than one ZDW allows multiple DWs to appear and span the SC bandwidth further [45]. In our case, eight ZDWs would generate up to four DWs. The spectral position of a DW can be estimated by evaluating the integrated dispersion  $\beta_{\rm int}$ ; i.e., the DWs appear near the wavelength of  $\beta_{\rm int} = 0$ . The  $\beta_{\rm int}$  is defined by [21],

$$\beta_{\text{int}} = \beta(\omega) - \beta(\omega_p) - (\omega - \omega_p)\beta'(\omega_p) \tag{3}$$

where,  $\beta(\omega_{\rm p})$  and  $\beta'(\omega_{\rm p})$  are the propagation constant and the first-order derivative of the  $\beta$ , respectively, at the pumping frequency  $\omega_{\rm D}$ . To estimate the spectral locations of DWs and the corresponding SC bandwidth of our coupled waveguide array, we swept the pump wavelength near the mode coupling wavelengths and plotted the map of  $\beta_{int}$  in Fig. 5(a); the y-axis indicates the pump wavelength  $\lambda_p$  and the x-axis shows the corresponding spectrum of the  $\beta_{int}$ . The white line in the diagonal indicates the pump wavelength, where  $\beta_{int} = 0$ . The other white lines or the intersection between blue and orange colors represent the spectral locations of the phase-matched DWs, i.e.,  $\beta_{int} = 0$ . The dispersion profile of the waveguide array is also plotted in Fig. 5(b), guiding the dispersion regimes of the pump wavelength  $\lambda_p$ . The anomalous dispersion regime (D>0) is shaded with the green color, and the other white background is the normal dispersion regime (D < 0). Notice that, in Fig. 5(a), there are a couple of regimes where they show four DWs. These regimes are located near the ZDWs in both normal and anomalous dispersions and are expected to generate SCs efficiently.

### IV. SUPERCONTINUUM GENERATIONS IN A WAVEGUIDE ARRAY WITH MULTIPLE MODE COUPLINGS

To examine the effectiveness of the SC generation with the dispersion engineered waveguide array, we numerically simulated the SCs using the Nonlinear Schrdinger Equation (NLSE). The NLSE depicts the development of the temporal electric field envelope E(z, t) considering the propagation loss, GVD, self-phase modulation, and self-steepening effects [7], [23]. The following generalized NLSE has been widely used to examine SC generations in different types of waveguides [18]–[20], [23], including waveguide arrays [13], [46], addressing experimental results fairly accurately. The generalized NLSE can be written as,

$$\frac{\partial \mathbf{E}(z,t)}{\partial z} + \frac{\alpha}{2} \mathbf{E}(z,t) - j \sum_{k>2} j^k \frac{\beta_k}{k!} \frac{\partial^k \mathbf{E}(z,t)}{\partial t^k}$$

$$= j\gamma \left( 1 + j\tau_{shock} \frac{\partial}{\partial t} \right) |\mathbf{E}(z,t)|^2 \mathbf{E}(z,t) \tag{4}$$

where,  $\alpha$  is the propagation loss,  $\beta_k$  is the k-th order chromatic dispersion derived from the Taylor expansion of the wavenumber  $\beta$ , and  $\gamma$  is the modal nonlinear coefficient. The time derivative term models the self-steepening and optical shock formation, which are characterized by  $\tau_{shock}$ . To address the frequency-dependent  $A_{\rm eff}$  in our waveguide array, a correction has been made to the  $\tau_{shock}$ , as follows [7],

$$\tau_{shock} = \tau_p + \frac{d}{d\omega} \left[ \ln \frac{1}{n_{\text{eff}}(\omega) A_{\text{eff}}(\omega)} \right]_{\omega_p}$$
(5)

where,  $\tau_p=1/\omega_p$ , with the angular pumping frequency  $\omega_p$ . The  $A_{\rm eff}(\omega)$  was obtained through the modal simulation. The Raman effect is weak in silicon nitride waveguides; thus, it has not been included in our model [22]. The NLSE was numerically solved using the split-step algorithm, assuming an input hyperbolic secant pulse with a full width at half maximum (FWHM) of 100-fs. We pumped in both normal and anomalous regions, considering a 0.45 dB/m propagation loss [24]. A short waveguide length of 10 mm is set to ensure the coherency.

#### A. Supercontinuums by Pumping in the Anomalous Dispersion

The dispersion of our waveguide array has four anomalous regions and we observed SC by pumping in each of them at  $\lambda_n^{a_i}$ ; the superscript  $a_i$  indicates the *i*-th anomalous region in the dispersion curve. Fig. 6(a-d) show the SC spectra by pumping in four different anomalous dispersion regions. The pump wavelength is marked by a red dashed vertical line in every case. The  $\beta_{\rm int}$  profiles pumping at each  $\lambda_p$  are plotted on the top panel of each Fig. 6(a-d) (with blue lines); they depict the positions of DWs, i.e., when  $\beta_{\rm int} = 0$ . The gray line on the same panel shows the dispersion profile and guides the dispersion of the pump wavelength. In Fig. 6(a), when  $\lambda_p^{a_1} = 1450$  nm, two DWs are observed simultaneously at around 190 pJ. The DW at a longer wavelength is away from the pump and required a higher power to transfer the energy across that DW. Ripples observed at a shorter wavelength are attributed to the soliton fission effect, by which the injected pulse is divided into distinct solitons, leading

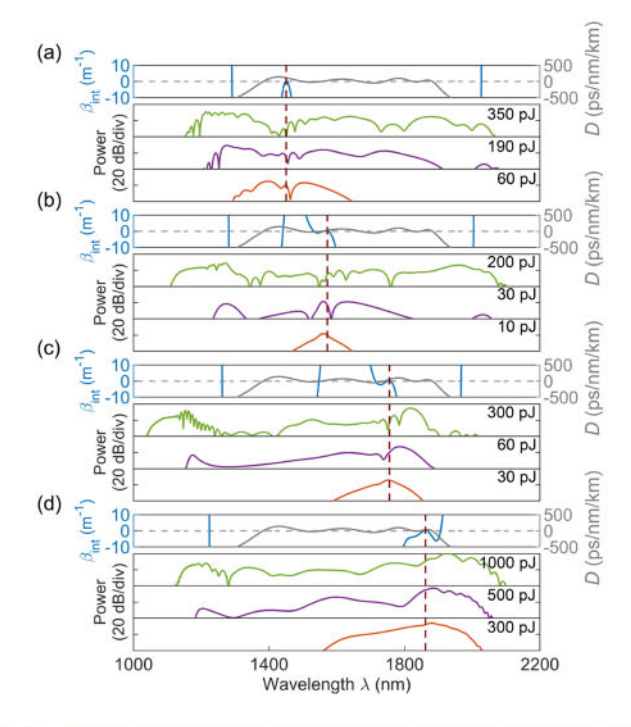


Fig. 6. Supercontinuum (SC) generation by pumping in the different anomalous dispersion regions. SC spectra pumping at (a)  $\lambda_p^{a,1}=1450$  nm, (b)  $\lambda_p^{a,2}=1560$  nm, (c)  $\lambda_p^{a,3}=1750$  nm, and (d)  $\lambda_p^{a,4}=1860$  nm. Each pump wavelength is marked with a vertical red dashed line. The integrated dispersion  $\beta_{\rm int}$  (blue) of each pump is plotted on the top of each panel of (a-d), together with the dispersion curve (gray). The waveguide lengths are set to 10 mm, and the pump energy is marked on each panel.

to spectral interference [21]. With a pump energy of 350 pJ, the SC spanned to a near-octave. In Fig. 6(b), we chose to pump near the ZDW at  $\lambda_p^{a_2} = 1560$  nm, which would allow an extended interaction length for a broader SC [45]. Three distinctive DWs are observed; one of them is at a wavelength longer than  $\lambda_p$ . With the multiple DWs near the pump, an efficient SC covering > 1000 nm is generated with a low pump of 200 pJ. In Fig. 6(c), we selected a pump wavelength close to the ZDW as well at  $\lambda_n^{a_3} = 1750$  nm. With pump energy as low as 60 pJ, a DW is generated at the shorter wavelength. However, even with a pump as high as 350 pJ, the DW in the longer wavelength is not seen clearly. This is because of the poor nonlinearity at longer wavelengths. The nonlinear coefficient  $\gamma$  is inversely proportional to the effective area  $A_{\text{eff}}$ , which increases with a higher-order mode. At a longer wavelength, the near-zero dispersion is induced with the TE<sub>3</sub> mode; thus, in turn,  $\gamma$  decreases with poor efficiency. For the same reason, the conversion efficiency of the SC pumping at  $\lambda_{\rm p}^{a_4} = 1860$  nm is quite poor (Fig. 6(d)); even with the input pulse energy of 300 pJ, the energy is not transferred to the DW in the short wavelength region. With pulse energy of 500 pJ, a prominent DW peak begins to be observed; then, pump energy as high as 1000 pJ is required to clearly see an octave-spanning SC spectrum.

# B. Supercontinuums by Pumping in the Normal Dispersion

Pumping in the normal dispersion regime leads to a coherent SC since the spectral broadening does not rely on soliton

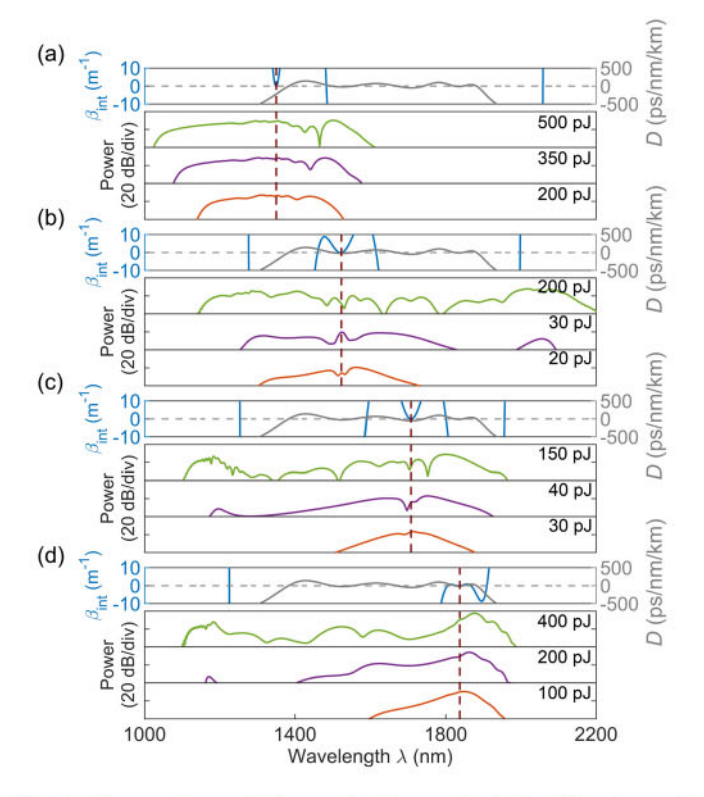


Fig. 7. Supercontinuum (SC) generation by pumping in the different normal dispersion regions. SC spectra pumping at (a)  $\lambda_p^{n_1}=1350$  nm, (b)  $\lambda_p^{n_2}=1525$  nm, (c)  $\lambda_p^{n_3}=1710$  nm, and (d)  $\lambda_p^{n_4}=1840$  nm. Each pump wavelength is marked with a vertical red dashed line. The integrated dispersion  $\beta_{\rm int}$  (blue) of each pump is plotted on the top of each panel of (a-d), together with the dispersion curve (gray). The waveguide lengths are set to 10 mm, and the pump energy is marked on each panel.

dynamics [25]; this is highly desired in self-referenced comb offset stabilization [47]. However, pumping in a normal regime results in a temporal broadening and rapid reduction of peak power, limiting the extent of nonlinear broadening [48]. In our case, the ZDWs are placed closely and quickly transfer the pump energy to the anomalous regime, which in turn creates a DW back in the normal regions away from the pump [49]. Fig. 7(a-d) show the SC spectra pumping at wavelengths of different normal dispersion regimes: (a)  $\lambda_p^{n_1}=1350$  nm, (b)  $\lambda_p^{n_2}=1525$  nm, (c)  $\lambda_p^{n_3}=1710$  nm, and (d)  $\lambda_p^{n_4}=1840$  nm. The superscript  $n_i$  indicates the *i*-th normal region in the dispersion curve. In Fig. 7(a), we pumped in a highly normal (-250 ps/nm/km)dispersion regime. Two DWs are expected with the  $\beta_{int}$  curve; however, only one DW near the pump is observed, due to the low nonlinearity at a longer wavelength regime. Notice that, even with high input energy, no ripples are observed in the generated SC spectrum, which indicates the absence of soliton fission. For the second case, as in Fig. 7(b), there are four DWs, two on each side of the pump. Two of the DWs are close to the pump and are not distinguishable in the SC spectrum. With a 30 pJ pump, a prominent peak is observed at ≈2000 nm, indicating the DW generation. With an increased pump, the spectrum becomes flattened with intermediate frequency components, and the SC spectrum extends to almost an octave (from 1100 nm to

2180 nm). In Fig. 7(c), a similar trend was observed; however, the DW at the longer wavelength was not prominent due to a lower nonlinearity in this regime. For the last case, in Fig. 7(d), a DW away from the pump is observed with a 200 pJ pump, but higher pump energy (400 pJ) is required to fill the spectral gap between the pump and the DW; again, this is due to the lower effective nonlinearity at a longer wavelength. Increasing the number of mode couplings would expand the bandwidth of flattened near-zero dispersion regions and increase the SC bandwidth. However, one may need to be careful in choosing the pump wavelength, as this scheme has a lower effective nonlinearity at a longer wavelength regime. The NLSE simulations suggest that pumping in near the ZDW, which is located in the slightly shorter wavelength regime of the near-zero dispersion band, generates the SCs most efficiently (e.g., as in the cases of Figs. 6(b) and 7(b)).

#### V. CONCLUSION

In summary, we proposed a thin silicon nitride waveguide array that excites multiple mode couplings with broadband NZD at NIR. The overall dispersion shows eight ZDWs in the nearinfrared, with a bandwidth of ≈550 nm, within ±90 ps/nm/km. The thin film thickness of the silicon nitride waveguide array makes it compatible with the current CMOS process, and its broadband NZD profile at NIR should be useful in diverse nonlinear applications. As an example, we numerically showed octave-spanning SC generation by pumping at both normal and anomalous dispersion regimes in the near-infrared. Our approach of using the multiple mode couplings to induce a broadband NZD can be applied to other spectral bands and material platforms as well, especially for mid-infrared SC and frequency comb generations for molecular sensing and spectroscopic applications [46].

#### REFERENCES

- R. Watt, C. Kaminski, and J. Hult, "Generation of supercontinuum radiation in conventional single-mode fibre and its application to broadband absorption spectroscopy," *Appl. Phys. B*, vol. 90, no. 1, pp. 47–53, 2008.
- [2] J. T. Woodward, A. W. Smith, C. A. Jenkins, C. Lin, S. W. Brown, and K. R. Lykke, "Supercontinuum sources for metrology," *Metrologia*, vol. 46, no. 4, pp. S277–S282, 2009.
- [3] M. A. Foster, A. L. Gaeta, Q. Cao, and R. Trebino, "Soliton-effect compression of supercontinuum to few-cycle durations in photonic nanowires," Opt. Express, vol. 13, no. 18, pp. 6848–6855, 2005.
- [4] K. E. Webb et al., "Nonlinear optics of fibre event horizons," National Commun., vol. 5, no. 1, pp. 1–7, 2014.
- [5] S. Moon and D. Y. Kim, "Ultra-high-speed optical coherence tomography with a stretched pulse supercontinuum source," *Opt. Express*, vol. 14, no. 24, pp. 11 575–11 584, 2006.
- [6] C. Lin and R. Stolen, "New nanosecond continuum for excited-state spectroscopy," Appl. Phys. Lett., vol. 28, no. 4, pp. 216–218, 1976.
- [7] J. M. Dudley, G. Genty, and S. Coen, "Supercontinuum generation in photonic crystal fiber," *Rev. Mod. Phys.*, vol. 78, no. 4, pp. 1135–1184, 2006.
- [8] G. P. Agrawal, "Nonlinear fiber optics," in Nonlinear Science at the Dawn of the 21st Century, Berlin, Heidelberg: Springer, 2000, pp. 195–211.
- [9] U. D. Dave et al., "Dispersive-wave-based octave-spanning supercontinuum generation in InGaP membrane waveguides on a silicon substrate," Opt. Lett., vol. 40, no. 15, pp. 3584–3587, 2015.
- [10] Y. Yu et al., "Experimental demonstration of linearly polarized 2–10 μm supercontinuum generation in a chalcogenide RIB waveguide," Opt. Lett., vol. 41, no. 5, pp. 958–961, 2016.

- [11] C. C. Evans, K. Shtyrkova, J. D. Bradley, O. Reshef, E. Ippen, and E. Mazur, "Spectral broadening in anatase titanium dioxide waveguides at telecommunication and near-visible wavelengths," *Opt. Express*, vol. 21, no. 15, pp. 18 582–18 591, 2013.
- [12] J. Yuan et al., "Mid-infrared octave-spanning supercontinuum and frequency comb generation in a suspended germanium-membrane ridge waveguide," J. Lightw. Technol., vol. 35, no. 14, pp. 2994–3002, 2017.
- [13] D. D. Hickstein et al., "Ultrabroadband supercontinuum generation and frequency-comb stabilization using on-chip waveguides with both cubic and quadratic nonlinearities," Phys. Rev. Appl., vol. 8, no. 1, pp. 1–8, 2017.
- [14] M. Yu, B. Desiatov, Y. Okawachi, A. L. Gaeta, and M. Lončar, "Coherent two-octave-spanning supercontinuum generation in lithium-niobate waveguides," Opt. Lett., vol. 44, no. 5, pp. 1222–1225, 2019.
- [15] R. K. Lau, M. R. Lamont, A. G. Griffith, Y. Okawachi, M. Lipson, and A. L. Gaeta, "Octave-spanning mid-infrared supercontinuum generation in silicon nanowaveguides," *Opt. Lett.*, vol. 39, no. 15, pp. 4518–4521, 2014.
- [16] N. Singh et al., "Octave-spanning coherent supercontinuum generation in silicon on insulator from 1.06 μm to beyond 2.4 μm," Light Sci. Appl., vol. 7, no. 1, pp. 17 131–17 131, 2018.
- [17] P. Koonath, D. R. Solli, and B. Jalali, "Continuum generation and carving on a silicon chip," Appl. Phys. Lett., vol. 91, no. 6, pp. 061111-1–061111-3, 2007.
- [18] A. R. Johnson et al., "Octave-spanning coherent supercontinuum generation in a silicon nitride waveguide," Opt. Lett., vol. 40, no. 21, pp. 5117–5120, 2015.
- [19] Y. Okawachi, M. Yu, J. Cardenas, X. Ji, M. Lipson, and A. L. Gaeta, "Coherent, directional supercontinuum generation," *Opt. Lett.*, vol. 42, no. 21, pp. 4466–4469, 2017.
- [20] M. A. Porcel et al., "Two-octave spanning supercontinuum generation in stoichiometric silicon nitride waveguides pumped at telecom wavelengths," Opt. Express, vol. 25, no. 2, pp. 1542–1554, 2017.
- [21] H. Guo et al., "Mid-infrared frequency comb via coherent dispersive wave generation in silicon nitride nanophotonic waveguides," Nat. Photon., vol. 12, no. 6, pp. 330–335, 2018.
- [22] A. Klenner et al., "Gigahertz frequency comb offset stabilization based on supercontinuum generation in silicon nitride waveguides," Opt. Express, vol. 24, no. 10, pp. 11 043–11 053, 2016.
- [23] H. Zhao et al., "Visible-to-near-infrared octave spanning supercontinuum generation in a silicon nitride waveguide," Opt. Lett., vol. 40, no. 10, pp. 2177–2180, 2015.
- [24] J. F. Bauters et al., "Planar waveguides with less than 0.1 db/m propagation loss fabricated with wafer bonding," Opt. Express, vol. 19, no. 24, pp. 24 090–24 101, 2011.
- [25] A. L. Gaeta, M. Lipson, and T. J. Kippenberg, "Photonic-chip-based frequency combs," *Nat. Photon.*, vol. 13, no. 3, pp. 158–169, 2019.
- [26] Y. Xuan et al., "High-Q silicon nitride microresonators exhibiting low-power frequency comb initiation," Optica, vol. 3, no. 11, pp. 1171–1180, 2016.
- [27] M. H. Pfeiffer et al., "Photonic damascene process for integrated high-Q microresonator based nonlinear photonics," Optica, vol. 3, no. 1, pp. 20–25, 2016.
- [28] X. Ji et al., "Ultra-low-loss on-chip resonators with sub-milliwatt parametric oscillation threshold," Optica, vol. 4, no. 6, pp. 619–624, 2017.
- [29] A. C. Turner et al., "Tailored anomalous group-velocity dispersion in silicon channel waveguides," Opt. Express, vol. 14, no. 10, pp. 4357–4362, 2006.
- [30] M. Zhu et al., "Ultrabroadband flat dispersion tailoring of dual-slot silicon waveguides," Opt. Express, vol. 20, no. 14, pp. 15 899–15 907, 2012.
- [31] L. Zhang, Y. Yue, R. G. Beausoleil, and A. E. Willner, "Flattened dispersion in silicon slot waveguides," *Opt. Express*, vol. 18, no. 19, pp. 20 529–20 534, 2010.
- [32] L. Zhang, Q. Lin, Y. Yue, Y. Yan, R. G. Beausoleil, and A. E. Willner, "Silicon waveguide with four zero-dispersion wavelengths and its application in on-chip octave-spanning supercontinuum generation," *Opt. Express*, vol. 20, no. 2, pp. 1685–1690, 2012.
- [33] Y. Guo et al., "Bilayer dispersion-flattened waveguides with four zerodispersion wavelengths," Opt. Lett., vol. 41, no. 21, pp. 4939–4942, 2016.
- [34] Y. Guo et al., "Ultra-flat dispersion in an integrated waveguide with five and six zero-dispersion wavelengths for mid-infrared photonics," Photon. Res., vol. 7, no. 11, pp. 1279–1286, 2019.
- [35] S. Kim et al., "Dispersion engineering and frequency comb generation in thin silicon nitride concentric microresonators," Nature Commun., vol. 8, no. 1, pp. 1–8, 2017.

- [36] G. Moille, Q. Li, S. Kim, and D. Westly, and K. Srinivasan, "Phased-locked two-color single soliton microcombs in dispersion-engineered Si<sub>3</sub> N<sub>4</sub> resonators," *Opt. Lett.*, vol. 43, no. 12, pp. 2772–2775, 2018.
- [37] S. Kim and M. Qi, "Broadband second-harmonic phase-matching in dispersion engineered slot waveguides," Opt. Express, vol. 24, no. 2, pp. 773–786, 2016.
- [38] S. Fatema, M. Mia, and S. Kim, "Broadband near-zero dispersion with multiple mode couplings," in *Proc. IEEE Photon. Conf. (IPC), San Anto*nio, TX, USA., 2019, pp. 1–2.
- [39] S. Ramelow et al., "Strong polarization mode coupling in microresonators," Opt. Lett., vol. 39, no. 17, pp. 5134–5137, 2014.
- [40] M. Mia, N. Jaidye, and S. Kim, "Extremely high dispersions in heterogeneously coupled waveguides," *Opt. Express*, vol. 27, no. 8, pp. 10 426–10 437, 2019.
- [41] U. Peschel, T. Peschel, and F. Lederer, "A compact device for highly efficient dispersion compensation in fiber transmission," *Appl. Phys. Lett.*, vol. 67, no. 15, pp. 2111–2113, 1995.
- [42] S. Kim and M. Qi, "Mode-evolution-based polarization rotation and coupling between silicon and hybrid plasmonic waveguides," Sci. Rep., vol. 5, pp. 1–7, 2015.
- [43] N. Akhmediev and M. Karlsson, "Cherenkov radiation emitted by solitons in optical fibers," *Phys. Rev. A*, vol. 51, no. 3, pp. 2602–2607, 1995.
- [44] A. E. Dorche, S. Abdollahramezani, H. Taheri, A. A. Eftekhar, and A. Adibi, "Extending chip-based kerr-comb to visible spectrum by dispersive wave engineering," *Opt. Express*, vol. 25, no. 19, pp. 22 362–22 374, 2017.
- [45] A. L. Gaeta, "Nonlinear propagation and continuum generation in microstructured optical fibers," Opt. Lett., vol. 27, no. 11, pp. 924–926, 2002.
- [46] H. Guo et al., "Nanophotonic supercontinuum-based mid-infrared dual-comb spectroscopy," Optica, vol. 7, no. 9, pp. 1181–1188, 2020.
- [47] H. R. Telle, G. Steinmeyer, A. Dunlop, J. Stenger, D. Sutter, and U. Keller, "Carrier-envelope offset phase control: A novel concept for absolute optical frequency measurement and ultrashort pulse generation," *Appl. Phys. B*, vol. 69, no. 4, pp. 327–332, 1999.
- [48] J. M. Dudley and J. R. Taylor, Supercontinuum Gener. Opt. Fibers. Cambridge University Press, 2010.
- [49] S. Roy, D. Ghosh, S. K. Bhadra, and G. P. Agrawal, "Role of dispersion profile in controlling emission of dispersive waves by solitons in supercontinuum generation," *Opt. Commun.*, vol. 283, no. 15, pp. 3081–3088, 2010

Saleha Fatema received the B.Sc. degree in electrical and electronic engineering from the Chittagong University of Engineering and Technology, Bangladesh, in 2016, and the M.S. degree in electrical engineering from Texas Tech University, Texas, USA, in 2020. She is currently working toward the Ph.D. degree in electrical and computer ngineering with Purdue University, West Lafayette, Indiana. Her research interests include integrated photonics, dispersion engineering, and quantum optics.

Md Borhan Mia (Student Member, IEEE) received the B.Sc. degree from the Bangladesh University of Engineering and Technology, Dhaka, Bangladesh, in 2016. He received the M.S. degree with the Department of Electrical and Computer Engineering of Texas Tech University, Texas, USA, in 2020. His research interests include high-density photonic integration, metamaterials, passive photonic devices, and inverse photonic designs.

Sangsik Kim (Senior Member, IEEE) is currently an Assistant Professor with the Department of Electrical and Computer Engineering (ECE) with Texas Tech University. Previously, he was a Postdoctoral Research Associate with the National Institute of Standards and Technology, Maryland, United States. He received the B.S. degree in ECE from Seoul National University, South Korea, in 2008. He was also a Postdoctoral Researcher with ECE, Purdue University, where he received the M.S. and Ph.D. degrees in 2014 and 2015, respectively.